Draft version October 15, 2019
Preprint typeset using LaTeX style emulateapj v. 08/22/09

MAGNETIC HELICITY DISSIPATION IN AN IDEAL MHD CODE

Axel Brandenburg[1,2,3,4] & Evan Scannapieco[5]
[1]Nordita, KTH Royal Institute of Technology and Stockholm University, Roslagstullsbacken 23, SE-10691 Stockholm, Sweden
[2]Department of Astronomy, AlbaNova University Center, Stockholm University, SE-10691 Stockholm, Sweden
[3]JILA and Laboratory for Atmospheric and Space Physics, University of Colorado, Boulder, CO 80303, USA
[4]McWilliams Center for Cosmology & Department of Physics, Carnegie Mellon University, Pittsburgh, PA 15213, USA
[5]Arizona State University, School of Earth and Space Exploration, P.O. Box 871404, Tempe, AZ 85287, USA

(Dated: Revision: 1.66)
Draft version October 15, 2019

ABSTRACT

We study a turbulent helical dynamo in a periodic domain by solving the ideal magnetohydrodynamic (MHD) equations with the `FLASH` code using the divergence-cleaning eight-wave method and compare our results with with direct numerical simulations (DNS) using the Pencil Code. At low resolution, `FLASH` reproduces the DNS results qualitatively by developing the large-scale magnetic field expected from DNS, but at higher resolution, no large-scale magnetic field is obtained. In all those cases in which a large-scale magnetic field is generated, the ideal MHD equations yield too little power at small scales. As a consequence, the small-scale current helicity is too small compared with the DNS. The resulting net current helicity has then always the wrong sign, and it also does not approach zero at late times, as expected from the DNS. Our results have implications for astrophysical dynamo simulations of stellar and galactic magnetism using ideal MHD codes.

Subject headings: dynamo — hydrodynamics — MHD — turbulence — Sun: corona, dynamo

1. INTRODUCTION

Astrophysical dynamos operate at large magnetic Reynolds numbers. This means that at large and moderately large scales, magnetic diffusion is negligible compared with the nonlinear terms. However, some level of magnetic diffusion and viscosity is still needed in numerical simulations to keep the code stable and to dissipate kinetic and magnetic energies into thermal energy. In numerical codes that solve the ideal magnetohydrodynamic (MHD) equations, this is accomplished by purely numerical means.

In spite of the comparatively small values of the magnetic diffusivity, the process of magnetic diffusion is an essential part of any dynamo, because the magnetic field evolution would otherwise be reversible. This is illustrated by what is called the stretch–twist–fold dynamo (Vainshtein & Zeldovich 1972; Childress & Gilbert 1995), where a little bit of diffusion is needed to "glue" the constructively folded structures together and prevent this flux rope arrangement from undoing itself. The need for having magnetic diffusion in a dynamo was also shown analytically in Moffatt & Proctor (1985). In fact, an ideal magnetic field evolution with strictly vanishing magnetic diffusivity can always be described in terms of the advection of two Euler potentials, but no dynamo solutions have ever been found by this method (Brandenburg 2010). In view of these complications, is it then still possible to solve the dynamo problem with an ideal MHD code? And even if it is possible, will the solution be wrong and if so, in what way?

There is a related question about the use of ideal MHD in solving the dynamo problem. Magnetic helicity is known to play an important role in certain types of dynamos, namely those that amplify a large-scale magnetic field via the α effect. Such dynamos are driven by kinetic helicity. This can produce a helical magnetic field, but since the magnetic helicity is conserved by the ideal MHD equations, this happens in such a way that there is magnetic helicity of opposite signs at different length scales (Seehafer 1996; Ji 1999). The question is therefore, whether ideal MHD codes can describe this evolution of magnetic helicity correctly.

Magnetic helicity conservation is an alien concept in numerical schemes designed to solve the ideal MHD equations. Such codes are primarily concerned with the conservation of mass, momentum, energy, and magnetic flux. Magnetic helicity, the volume integral of the magnetic field dotted into its inverse curl, i.e., the magnetic vector potential, is not normally considered. At large magnetic Reynolds numbers or at high conductivity, magnetic helicity changes only through fluxes (Berger & Field 1984). Those can occur under inhomogeneous conditions or in the presence of suitable boundary conditions.

Most code benchmarks are concerned with one- and two-dimensional test problems. In those cases, the magnetic helicity vanishes from the outset. We therefore need to resort to more complex three-dimensional problems to see the effects of magnetic helicity and its dissipation properties. A suitable benchmark that satisfies the aforementioned constraints is the homogeneous helical dynamo problem in a periodic domain. It produces large-scale magnetic fields through the α effect, but the resulting magnetic helicity at large scales must have the opposite sign to that of the kinetic helicity. However, when the magnetic field at the wavenumber of the energy-carrying eddies, k_f, reaches equipartition and saturates, the energy of the large-scale magnetic field is still weak compared to the field at k_f. The only way the large-scale magnetic field can grow further is by dissipating magnetic helicity. This should allow us to infer the rate of magnetic helicity dissipation. The amplitude of the large-scale magnetic field is also controlled by the evolution and destruction of magnetic helicity. This allows us to infer the effective scale dependence of the numerical diffusion operator.

When magnetic helicity dissipation is accomplished by Spitzer resistivity, the dissipation rate is proportional to the current helicity. The evolution of magnetic helicity is then given by

$$\frac{\mathrm{d}}{\mathrm{d}t}\langle \boldsymbol{A}\cdot\boldsymbol{B}\rangle = -2\eta\langle \boldsymbol{J}\cdot\boldsymbol{B}\rangle, \tag{1}$$

where $\boldsymbol{B}=\boldsymbol{\nabla}\times\boldsymbol{A}$ is the magnetic field in terms of the magnetic vector potential $\boldsymbol{A}$, and $\boldsymbol{J}=\boldsymbol{\nabla}\times\boldsymbol{B}$ is proportional to the current density. As can be seen from Equation (1), the current helicity $\langle \boldsymbol{J}\cdot\boldsymbol{B}\rangle$ must vanish once a steady state is reached (Brandenburg 2001). Again, this steady state is accompanied by a balance of large-scale and small-scale contributions of opposite signs. Under isotropic conditions, the current helicity at a certain wavenumber k is equal to the spectral magnetic helicity times k^2, because the former contains two more derivatives than the latter. However, if magnetic helicity dissipation is accomplished through other numerical processes, for example through hyperdiffusion, which has a steeper dependence on the wavenumber, then this can affect the magnetic helicity balance and therefore the final saturation value. This was demonstrated numerically by Brandenburg & Sarson (2002). Thus, a helically-driven dynamo may be an excellent system to study the properties of magnetic helicity dissipation, especially when this is accomplished only through numerical processes.

It is useful to begin with models whose numerical resolution is relatively small. In fact, even a resolution of just 32^3 mesh points is enough to find large-scale dynamo action; see Brandenburg (2001) for early models of that type. His simulations showed that, at higher resolution, and thus at larger magnetic Reynolds numbers, it takes progressively longer to reach the final saturation state of such a system with periodic boundary conditions.

In this paper, the first motivate and describe the details of our model (Section 2), and then present the results for the magnetic field evolutions at different numerical resolutions and compare in some cases with results of direct numerical simulations (DNS); see Section 3. We present concluding remarks in Section 4.

2. THE MODEL

2.1. *Periodic boundary conditions*

We consider here the arguably simplest setup of a large-scale turbulent dynamo. We drive turbulence through helical isotropic random forcing, which leads to an α effect. It is responsible for driving what in a sphere would be called poloidal and toroidal fields, so the resulting system is called an α^2 dynamo. We adopt periodic boundary conditions, as is commonly done in numerical studies of hydrodynamic and MHD turbulence.

We should emphasize from the outset that it is this assumption of periodicity that is primarily responsible for causing features of this dynamo that would not occur in astrophysical setups, namely the generation of a superequipartition magnetic field and a resistively slow evolution toward this final state (Brandenburg 2001). In real systems that are not periodic, magnetic helicity fluxes are believed to be important in high magnetic Reynolds number turbulence (Blackman & Field 2000). Those fluxes can prevent a resistively slow evolution while still allowing the system to saturate at approximately the equipartition field strength (Brandenburg 2018). Here, however, we are interested in quantifying the extent to that non-ideal effects play a role in an ideal MHD code, and so periodic boundary conditions are appropriate.

2.2. *Setup of the model*

We adopt a cubic domain of side length $L=1$, so the smallest wavenumber in the domain is $k_1=2\pi$. We solve the compressible MHD equations with a forcing function $\boldsymbol{f}$ on the right-hand side of the momentum equation. This forcing function is random in space and time, but has a characteristic wavenumber k_f that we choose to be larger than k_1 by a certain factor. The forcing function has positive helicity, so $\langle \boldsymbol{f}\cdot\boldsymbol{\nabla}\times\boldsymbol{f}\rangle/k_\mathrm{f}\langle \boldsymbol{f}^2\rangle$ is positive and close to unity.

2.3. *Code and choice of parameters*

We use `FLASH`[1] (Fryxell et al. 2000), to solve the equations for an isothermal gas, choosing a ideal gas with a $\gamma=1$ equation of state. The sound speed is unity, so the root-mean square (rms) value of the velocity $\boldsymbol{u}$ is automatically equal to the Mach number. We force the flow such that it remains subsonic on average with $u_\mathrm{rms}\approx 0.3$.

We use gaussian units, so the magnetic energy is given by $\mathcal{E}_\mathrm{M}=\langle \boldsymbol{B}^2\rangle/8\pi$, where $\boldsymbol{B}$ is the magnetic field. The density ρ is initially unity. Furthermore, because no mass enters or leaves the domain, the mean density remains always unity.

We use the MHD eight-wave module of `FLASH` (Derigs et al. 2016), which is based on a divergence-cleaning algorithm. The forcing function is analogous to that used by Sur et al. (2014), except that here only one sign of helicity is used. In particular, we used an artificial forcing term F which is modeled as a stochastic Ornstein-Uhlenbeck process (Eswaran & Pope 1988; Benzi et al. 2008) with a user-specified forcing correlation time, which was taken to be one half. In the following, we consider two values for the scale separation ratio k_f/k_1: a smaller one with a combination of 76 wavevectors with wavenumbers between 2 and 3, and a larger one with 156 wavevectors with wavenumbers between 4 and 5. These cases are distinguished by their average nominal forcing wavenumbers of 2.5 and 4.5, respectively.

3. RESULTS

3.1. *Weak scale separation*

In Figure 1, we plot the growth of $\mathcal{E}_\mathrm{M}$, normalized by the kinetic energy, $\mathcal{E}_\mathrm{K}=\langle\rho\boldsymbol{u}^2\rangle/2$, for different numerical resolutions. Time is given both in code units and in eddy turnover times, $(u_\mathrm{rms}k_\mathrm{f})^{-1}$. Ignoring density fluctuations, we define $u_\mathrm{rms}=(2\mathcal{E}_\mathrm{K})^{1/2}$, evaluated during the saturated phase of the dynamo. In all cases, the initial exponential growth phase is the same and the growth rate of the rms magnetic field (proportional to $\mathcal{E}_\mathrm{M}^{1/2}$) is $\lambda\approx 0.18$ in code units, corresponding to $\lambda/u_\mathrm{rms}k_\mathrm{f}\approx 0.036$ in units of the turnover rate. The magnetic energy saturates approximately at the equipartition level with $\mathcal{E}_\mathrm{M}\approx\mathcal{E}_\mathrm{K}$.

[1] `http://flash.uchicago.edu/site/flashcode/`

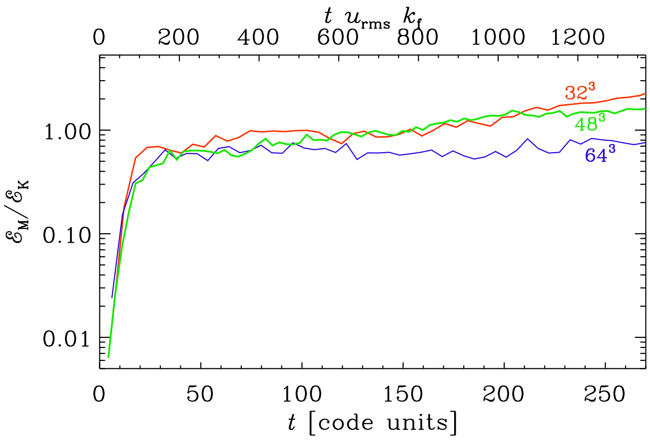

FIG. 1.— Early evolution of the normalized magnetic energy for resolutions 32^3, 48^3, 64^3 and $k_{\rm f}=2.5$. The upper abscissa gives time in eddy turnover times based on the run with 48^3.

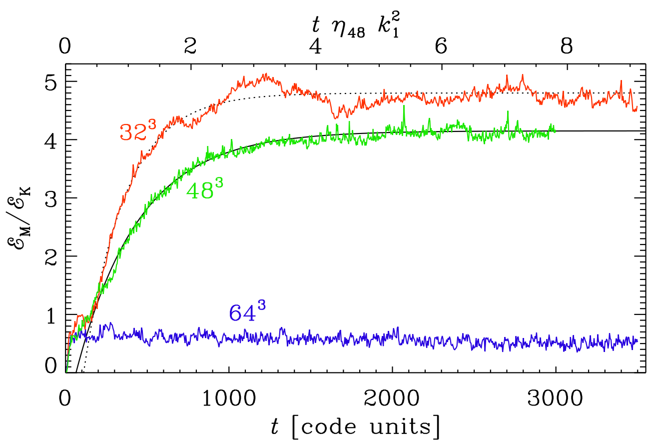

FIG. 2.— Saturation for resolutions 32^3, 48^3, 64^3 and $k_{\rm f}=2.5$. The upper abscissa gives time in microphysical diffusion times based on the run with 48^3.

The magnetic field evolution shown in Figure 1 is only the early saturation phase. At later times, the magnetic energy continues to increase for two of the runs, as shown in Figure 2. In fact, the system reaches values that exceed $\mathcal{E}_{\rm K}$ by a factor of 4–5.

Following Brandenburg (2001), we fit the late-time evolution of the magnetic energy to a curve of the form

$$\mathcal{E}_{\rm M}-\mathcal{E}_{\rm K}\approx\mathcal{E}_{\rm K}\,\frac{k_{\rm f}^{\rm eff}}{k_1}\left[1-e^{-2\eta k_1^2(t-t_{\rm sat})}\right]\quad\text{for } t>t_{\rm sat},\qquad(2)$$

where $k_{\rm f}^{\rm eff}$ and $t_{\rm sat}$ are fit parameters that characterize the effective forcing wavenumber and the effective saturation time, respectively (see Appendix A for a derivation). In the simulations in which η is formally zero, we also replace η by $\eta^{\rm eff}$ as an effective parameter that can be obtained from a fit to the evolution of $\mathcal{E}_{\rm M}(t)$. These parameters are listed in Table 1, along with other parameters characterizing the simulations. In particular, we also compare with the estimated *turbulent* magnetic diffusivity, $\eta_{\rm t0}=u_{\rm rms}/3k_{\rm f}$ (see, e.g. Blackman & Brandenburg 2002). The ratio $3\eta_{\rm t0}/\eta^{\rm eff}$ corresponds to the magnetic Reynolds number. In a few cases, however, we also add an explicit magnetic diffusivity; see the column denoted in Table 1 by η_{-6}. Those runs will be discussed separately in Sect. 3.3.

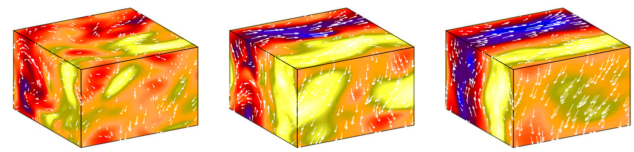

FIG. 3.— Visualizations of B_x and vectors of $\boldsymbol{B}$ (in white) on the periphery of the domain at times 200, 300, and 3500. Yellow (blue) shades denote positive (negative) values.

As we see from Table 1, the value of $k_{\rm f}^{\rm eff}$ does not vastly exceed the nominal value of $k_{\rm f}$. This is somewhat surprising, given that one would have expected that the numerical diffusion operator might be more efficient at high wavenumbers, as is the case with hyperdiffusion; see the corresponding numerical experiments of Brandenburg & Sarson (2002). This is apparently not the case. In some of the runs with explicit diffusion, however, there are cases where $k_{\rm f}^{\rm eff}$ exceeds the nominal value of $k_{\rm f}$ by a factor of 3–5.

There are two more fit parameters. One is $\eta^{\rm eff}$, which is inferred from a fit to the saturation behavior given by Equation (2). Its values are found to be small by comparison with the product $u_{\rm rms}\delta x\approx 5\times10^{-3}$, where $\delta x=1/32$ is the mesh spacing. The other fit parameter is $t_{\rm sat}$, whose values are listed for completeness; they characterize merely the time when the early saturation phases ends and this depends also on the value of the initial field. It is therefore not a parameter characterizing the numerical diffusion scheme. It turns out to be about the same for the 48^3 and 32^3 runs.

In Figure 3, we show a visualization of B_x on the periphery of the computational domain at selected times during the late saturation phase. We see that, at late times, B_x shows a sinusoidal variation in the y direction. There is also a similar variation of B_z, but it is phase shifted by 90° relative to B_x and not shown here. This type of field structure is one of three possible field configurations that all have negative magnetic helicity; see Brandenburg (2001) for details.

In Figure 4, we show magnetic energy spectra, $E_{\rm M}(k,t)$, at different times. They are normalized such that

$$\int_0^\infty E_{\rm M}(k,t)\,{\rm d}k=\mathcal{E}_{\rm M}(t),\qquad(3)$$

is the mean magnetic energy density. We clearly see that

TABLE 1
PARAMETERS OF THE VARIOUS RUNS.

Res	$k_{\rm f}$	$u_{\rm rms}$	$k_{\rm f}^{\rm eff}$	$t_{\rm sat}$	η_{-6}	$\eta_{-6}^{\rm eff}$	$3\eta_{\rm t0}/\eta^{\rm eff}$
32^3	2.5	0.28	3.8	170	0	50	360
48^3	2.5	0.30	3.2	170	0	66	270
64^3	2.5	0.30	—	—	0	—	—
64^3	2.5	0.25	11.7	5	5	34	470
32^3	4.5	0.28	8.0	60	0	100	150
48^3	4.5	0.29	—	—	0	—	—
64^3	4.5	0.30	—	—	0	—	—
64^3	4.5	0.25	12.1	5	5	64	140
64^3	4.5	0.21	4.7	10	50	150	49

All quantities are in code units; η_{-6} and $\eta_{-6}^{\rm eff}$ denote values in units of 10^{-6}.

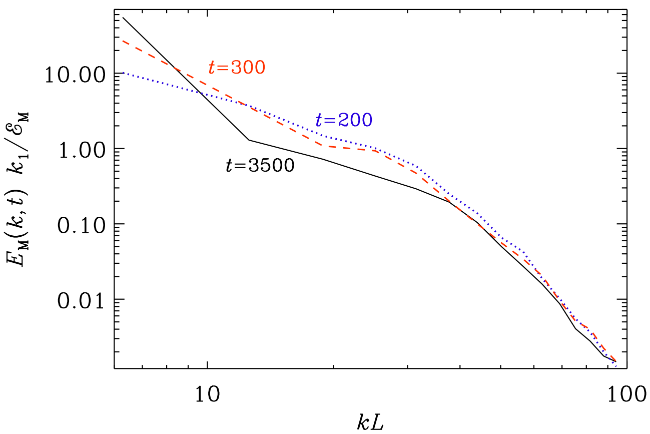

FIG. 4.— Magnetic energy spectra at times 200, 300, and 3500.

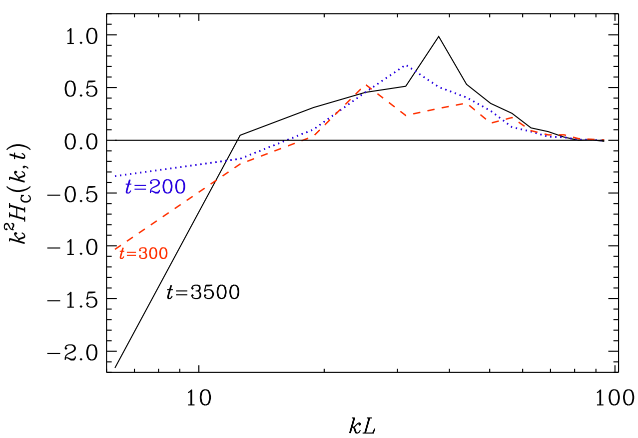

FIG. 5.— Current helicity dissipation spectra, $k^2 H_C(k,t)$, at times 200, 300, and 3500.

most of the magnetic energy is at the smallest possible wavenumber, $k = k_1$, corresponding to the largest possible scale of the system. In this case, the spectra show no particular feature at the forcing wavenumber. This may partly be caused by the relatively small scale separation ratio, i.e., k_f is not very large compared to k_1. Another reason may be the small resolution of only 32^3 mesh points. The largest wavenumber in the domain is the Nyquist wavenumber, $k_{Ny} = \pi/\delta x = \pi N/L \approx 100$ for this resolution, and ≈ 100 for 64^3 mesh points. Corresponding current helicity spectra, $H_C(k,t)$, scaled with k^2, are shown in Figure 5. Note that $H_C(k,t)$ is normalized such that $\int H_C\,dk = \langle \boldsymbol{J}\cdot\boldsymbol{B}\rangle$, where $\boldsymbol{J} = \boldsymbol{\nabla}\times\boldsymbol{B}$ is proportional to the current density. The scaling with k^2 has been adopted so that the high wavenumber part of the spectrum can be seen more clearly. Theoretically, however, we would have expected that, at late times, $\langle \boldsymbol{J}\cdot\boldsymbol{B}\rangle = 0$, so that the positive and negative parts of H_C should cancel, but not those of $k^2 H_C$; see Appendix A.

Our higher resolution run with 64^3 mesh points does not develop a large scale magnetic field. The resulting magnetic energy spectrum is shown in Figure 6. The magnetic energy spectrum is seen to peak at $kL \approx 30$, which corresponds to $k/k_1 \approx 5$. This is twice as large

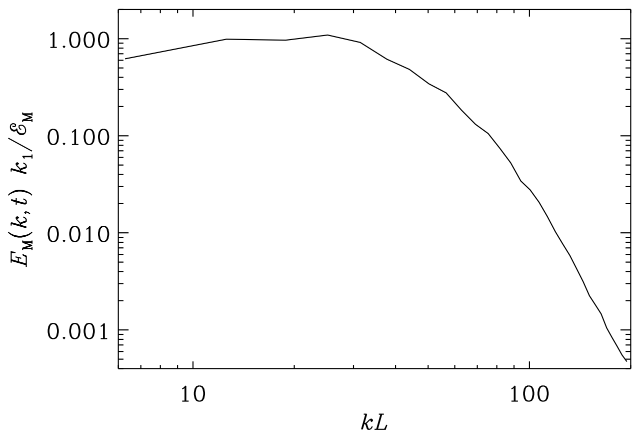

FIG. 6.— Spectra for the higher resolution run with 64^3 mesh points at time 3500, i.e., the end of the run.

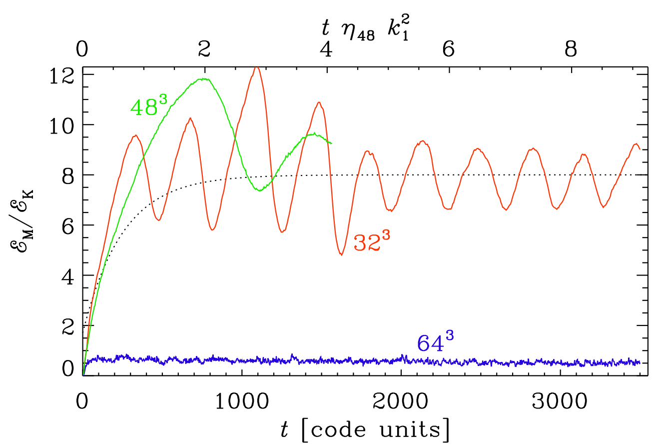

FIG. 7.— Late saturation for resolutions 32^3, 48^3, 64^3 and $k_f/k_1 = 4.5$. The upper abscissa gives time in microphysical diffusion times based on the empirical value η_{48} found for the run with 48^3 mesh points.

as the value of $k_f/k_1 = 2.5$. Such behavior is typical of small-scale dynamo action (Schekochihin et al. 2004).

3.2. *Larger scale separation ratio*

We have increased the value of k_f to include wavenumbers between 4 and 5. This scale separation ratio is still not very large, but we should keep in mind that the resolution is not very large either, and k_{Ny}/k_1 is only 16 for our 32^3 simulations. The results turn out to be quite different in many ways: first, the mean magnetic energy density shows oscillatory behavior (Figure 7) and second, the magnetic field develops a large-scale component already very early on. This behavior is rather unexpected. We also see that in the kinematic phase, the magnetic energy grows slightly faster than in the case of a smaller scale separation ratio. For the run with 64^3 mesh points, there is again no large-scale dynamo. Furthermore, normalized by the kinetic energy, the magnetic energy generated by the small-scale dynamo is now about half as strong as in the case with $k_f/k_1 = 2.5$. This can be explained by the fact that the effective magnetic Reynolds number based on the value of k_f is now smaller.

In Figure 8, we show the evolution of current helicity,

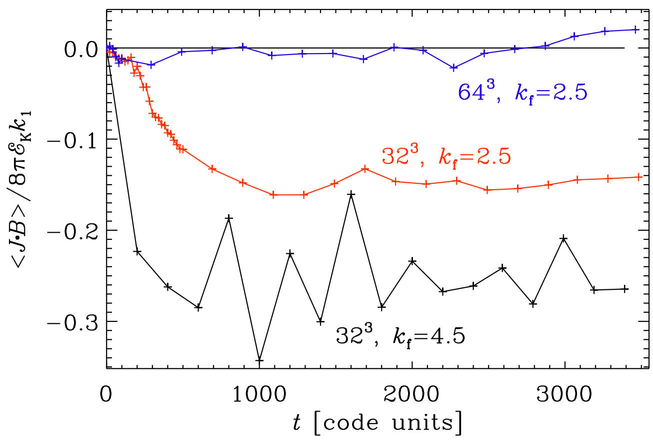

FIG. 8.— Evolution of current helicity for runs with different resolutions (32^3, 64^3) and different scale separation ($k_\mathrm{f}/k_1 = 2.5$ and 4.5).

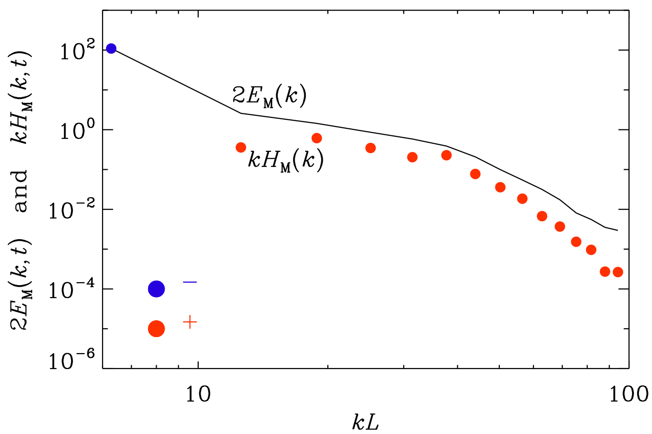

FIG. 9.— Comparison of magnetic energy and helicity spectra for the run with 32^3 mesh points and $k_\mathrm{f}/k_1 = 2.5$ at $t = 3500$. Positive (negative) values of H_M are plotted as red (blue) symbols.

$\langle \boldsymbol{J}\cdot\boldsymbol{B}\rangle$ for runs with different resolutions (32^3, 64^3) and different scale separation ($k_\mathrm{f}/k_1 = 2.5$ and 4.5). Except for the run with 64^3 mesh points and $k_\mathrm{f}/k_1 = 2.5$, where $\langle \boldsymbol{J}\cdot\boldsymbol{B}\rangle$ is seen to fluctuate around zero, we find a clear evolution away from zero with subsequent saturation at a negative value for the other two runs. It is therefore clear that the numerical evolution of magnetic helicity is – unlike the proper resistive case – not simply controlled by the value of the current helicity, because a finite value of $\langle \boldsymbol{J}\cdot\boldsymbol{B}\rangle$ should continue to drive magnetic helicity, $\langle \boldsymbol{A}\cdot\boldsymbol{B}\rangle$, to a new state all the time; see Appendix A. Here, $\boldsymbol{A}$ is the magnetic vector potential with $\boldsymbol{B} = \boldsymbol{\nabla}\times\boldsymbol{A}$.

To compute magnetic helicity spectra, $H_\mathrm{M}(k,t)$, we make use of the fact that, under isotropic conditions, $H_\mathrm{M}(k,t)$ is related to the current helicity spectrum $H_\mathrm{C}(k,t)$ via $H_\mathrm{M}(k,t) = H_\mathrm{C}(k,t)/k^2$. For the spectrum shown in Figure 9, we have verified this relation by computing $H_\mathrm{M}(k,t)$ directly from $\boldsymbol{A}$ in Fourier space (indicated by tildes) as $\tilde{A}_i = \epsilon_{ijl}\,\mathrm{i}k_j\tilde{B}_l/k^2$. It is normalized analogously to H_C as $\int H_\mathrm{M}(k,t)\,\mathrm{d}k = \langle \boldsymbol{A}\cdot\boldsymbol{B}\rangle$. In Figure 9, we compare the magnetic energy with the scaled magnetic helicity spectrum for the run with 32^3 mesh points and $k_\mathrm{f}/k_1 = 2.5$ at $t = 3500$ (in code units).

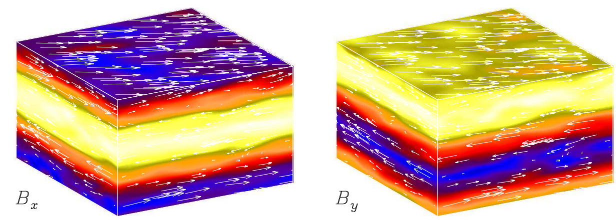

FIG. 10.— B_x and B_y at time 200 (in code units) for $k_\mathrm{f}/k_1 = 4.5$. Note that the fields now vary with z, and that the phases of B_x and B_y are shifted by 90° relative to each other. Yellow (blue) shades denote positive (negative) values.

We see that the spectral magnetic helicity is negative for $k = k_1$ and positive for all larger values of k, except for one data point near the Nyquist wavenumber.

In Figure 10, we show visualizations of B_x and B_y for $k_\mathrm{f}/k_1 = 4.5$ and 32^3 mesh points. A large-scale magnetic field develops very quickly. Unlike the case shown in Figure 3, the mean magnetic field now varies in the z direction and is here, except for an insignificant overall phase shift, of the form $\overline{\boldsymbol{B}} = (\cos k_1 z, \sin k_1 z, 0)$.

3.3. *Runs with explicit magnetic diffusivity*

`FLASH` allows for the possibility of adding an explicit magnetic diffusivity η. We now present simulations using for η the effective value of 5×10^{-5} found in the 32^3 simulations with $k_\mathrm{f}/k_1 = 2.5$. In this case we carry out simulations with 64^3 mesh points, where previously no large-scale magnetic field was found with `FLASH`. We also include a run with $\eta = 5\times10^{-5}$. In Figure 11, we show the results for $k_\mathrm{f}/k_1 = 2.5$ and 4.5.

It turns out that there is large-scale magnetic field growth in the case with $k_\mathrm{f}/k_1 = 4.5$ and $\eta = 5\times10^{-5}$, but not for 5×10^{-5} or more, and also not for $k_\mathrm{f}/k_1 = 2.5$. In both cases, however, there is large-scale dynamo action with $\eta = 5\times10^{-6}$. Interestingly, the value of η^eff is always larger than that of η by a factor of 3 to 13; see Table 1.

To understand the absence of large-scale dynamo action for $k_\mathrm{f}/k_1 = 2.5$ and $\eta = 5\times10^{-5}$, we must remember that k_f/k_1 must exceed a certain limit, which Haugen et al. (2004) found to be around 2.2; see their Figure 23. Whether the smallness of k_f is indeed the reason for the absence of dynamo action in our case with $k_\mathrm{f}/k_1 = 2.5$ cannot be conclusively answered and requires more dedicated tests with the PENCIL CODE, which are described next.

3.4. *Comparison with the* PENCIL CODE

We now compare with DNS results obtained with the PENCIL CODE.[2]. Again, we use $\eta = 5\times10^{-5}$ along with our two values of k_f/k_1, namely 2.5 and 4.5. In both cases, we find large-scale dynamo action. As expected, the amplitudes are different; compare the values of $k_\mathrm{f}^\mathrm{eff}$ for the different values of k_f in Table 2. The kinematic growth rate varies between $\lambda = 0.15$ and 0.30, which is compatible with the value of 0.18 obtained with `FLASH`.

Given that we perform DNS without subgrid scale modeling, there is a limit to the smallest value of ν that can be used at the resolutions adopted here, which are

[2] `https://github.com/pencil-code`

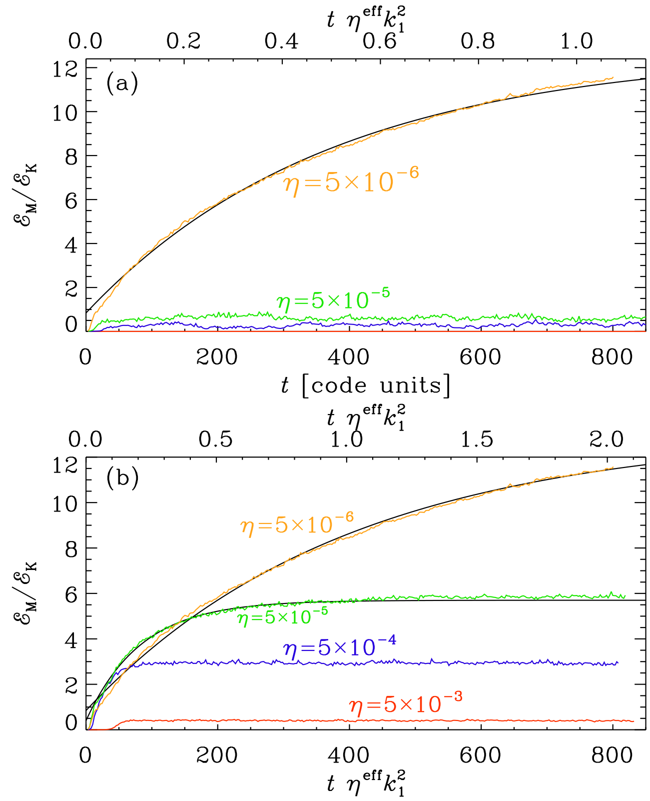

FIG. 11.— Saturation for runs with explicit magnetic diffusivity using (a) $k_{\rm f}/k_1 = 2.5$ and (b) $k_{\rm f}/k_1 = 4.5$ with $\eta = 5\times10^{-3}$ (red), 5×10^{-4} (blue), 5×10^{-5} (green), and 5×10^{-5} (orange), all at a resolution of 64^3 mesh points. The upper abscissa gives time in effective microphysical diffusion times based on the runs with the largest saturation value.

32^3 or 64^3 mesh points. It turns out that in all cases with $\eta = 5\times10^{-5}$ and $\nu = 5\times10^{-4}$, the code produces acceptable results for $t \lesssim 2000$ time units, but the code crashes at later times. This problem disappears when the viscosity is increased to $\nu = 2\times10^{-3}$, while $\eta = 5\times10^{-5}$ is kept unchanged. The corresponding values of the magnetic Prandtl number, $\mathrm{Pr_M} \equiv \nu/\eta$ are given in Table 2. We see that the results for $k_{\rm f}^{\rm eff}$ are not very sensitive to the value of ν.

It is important to realize that in DNS, there is no $\eta^{\rm eff}$, because the coefficient entering in Equation (2) is always the same as the input parameter η used. In all cases, the fit works well and there is no spurious diffusivity entering the resistively slow saturation phase. This is different in the `FLASH` code, where $\eta^{\rm eff}$ tends to exceed η by a factor

TABLE 2
PARAMETERS OF RUNS WITH THE PENCIL CODE.

Res	$k_{\rm f}$	$\mathrm{Pr_M}$	$u_{\rm rms}$	$k_{\rm f}^{\rm eff}$	$t_{\rm sat}$	$3\eta_{\rm t0}/\eta$
32^3	2.2	10	0.11	1.40	120	81
32^3	2.6	10	0.11	1.76	110	81
32^3	4.5	10	0.11	3.20	70	78
64^3	4.5	10	0.12	3.86	90	82
64^3	4.5	20	0.10	4.15	105	70
64^3	4.5	40	0.08	4.20	150	55

In all cases, $\eta^{\rm eff} = \eta = 5\times10^{-5}$, and $\mathrm{Re_M} = 3\eta_{\rm t0}/\eta$.

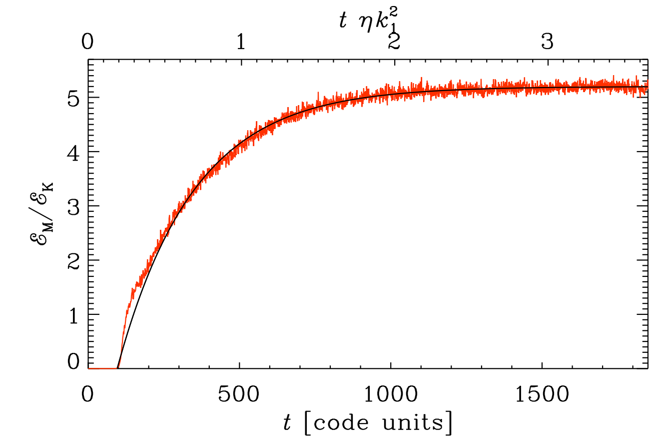

FIG. 12.— Direct numerical simulations with the PENCIL CODE using $\eta = 5\times10^{-5}$ and $k_{\rm f}/k_1 = 4.5$.

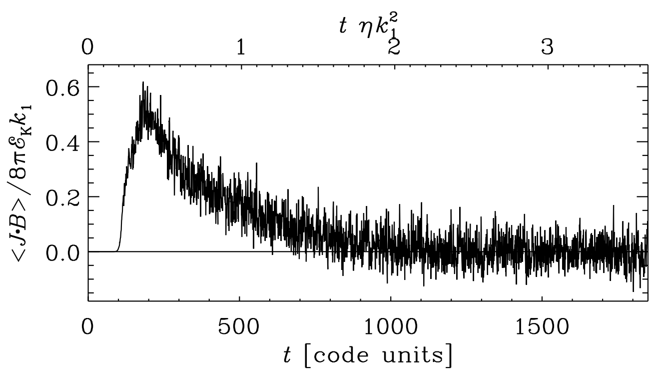

FIG. 13.— Evolution of $\langle \boldsymbol{J}\cdot\boldsymbol{B}\rangle$ for the run of Figure 12.

of 3 to 13.

As discussed above, $\langle \boldsymbol{J}\cdot\boldsymbol{B}\rangle$ should approach zero at late times. This is shown in Figure 13, which demonstrates that $\langle \boldsymbol{J}\cdot\boldsymbol{B}\rangle$ is initially zero, begins to rise after about 100 time units, reaches then a positive maximum after about one third of a diffusion time, and then decays to zero on a resistive time scale. It is interesting to note that $\langle \boldsymbol{J}\cdot\boldsymbol{B}\rangle$ is positive, while in the ideal simulations with `FLASH`, it has a negative value; see Figure 8.

Looking at the corresponding magnetic energy spectrum of Figure 9 with `FLASH`, we see that there is a strong dominance of the large-scale field over the small-scale field. This is also consistent with the corresponding current helicity spectra shown in Figure 5, keeping in mind that we scaled $H_{\rm C}(k,t)$ with k^2 to show the rather weak contributions from small scales. Thus, we can conclude that the reason for the wrong sign of $\langle \boldsymbol{J}\cdot\boldsymbol{B}\rangle$ in the `FLASH` code is its inability to reproduce the relative strengths of small-scale and large-scale fields correctly.

3.5. *Total magnetic helicity production*

An important question concerns the total magnetic helicity production during the early small-scale and later large-scale dynamo processes. We quantify this in terms of the evolution of the fractional magnetic helicity defined as $\langle \boldsymbol{A}\cdot\boldsymbol{B}\rangle k_1/\langle \boldsymbol{B}^2\rangle$, which is always between $+1$ and -1; see, e.g., Kahniashvili et al. (2010). Its evolution is shown in Figure 14, where we compare the results

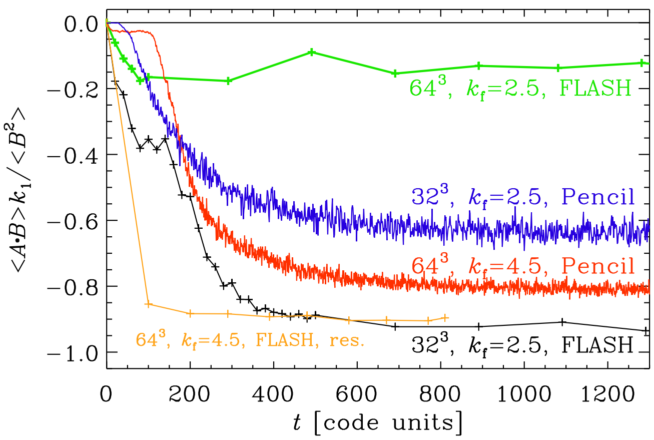

FIG. 14.— Evolution of the fractional magnetic helicity for the case with 32^3 mesh points, $k_\mathrm{f}/k_1 = 2.5$, and $\eta^\mathrm{eff} = 5 \times 10^{-5}$ (black line), compared with the evolution in DNS with 32^3 mesh points, $k_\mathrm{f}/k_1 = 2.5$, and $\eta = 5 \times 10^{-5}$ (blue). Also shown are a DNS with 64^3 mesh points ($k_\mathrm{f}/k_1 = 4.5$, $\eta = 5 \times 10^{-5}$, red line), and a solution with `FLASH` with explicit resistivity ($k_\mathrm{f}/k_1 = 4.5$, $\eta = 5 \times 10^{-5}$, orange line).

from ideal simulations with those of DNS. We find that both simulations produce negative magnetic helicity, but the `FLASH` code reaches about 90%, while the expected value from the DNS is only about 60%. By comparison, even with a larger scale separation of $k_\mathrm{f}/k_1 = 4.5$ instead of 2.5, we still only obtain about 80% in the DNS. This supports our earlier conclusion that the `FLASH` code produces too much power at large length scales.

We also see that, even at early times, the `FLASH` code produces already nearly 40% magnetic helicity with 32^3 mesh points and about 15% with 64^3 mesh points. The expected value based on the DNS is basically zero when $k_\mathrm{f}/k_1 = 2.5$, and about 2–3% when $k_\mathrm{f}/k_1 = 4.5$. This difference at these early times is particularly remarkable, because this is still the phase when the slow resistive evolution did not yet have time to act. It is even worse in the run with explicit magnetic diffusivity, were a fractional helicity of 90% is generated almost immediately.

4. DISCUSSION

Our study has shown qualitative agreement between earlier resistive simulations and the present ideal MHD simulations when both the resolution is small (32^3 or 48^3 mesh points) and the forcing wavenumber is small ($k_\mathrm{f}/k_1 = 2.5$). At higher resolution (64^3 mesh points), we find no large-scale dynamo action at all (neither at $k_\mathrm{f}/k_1 = 2.5$ nor at 4.5). Of course, given that the ambition of an ideal MHD code is to reproduce the results for zero resistivity, our finding of no large-scale dynamo activity at 64^3 mesh points is, in principle, the correct one, i.e., the magnetic helicity stays zero, and as a consequence also the current helicity never changes. It is curious, however, that the change between our 48^3 and 64^3 results is so abrupt. Furthermore, the qualitatively different behavior in the form of oscillations found by increasing k_f/k_1 from 2.5 to 4.5, is also rather surprising. In addition, as we just saw, the magnetic helicity is not really zero in the 64^3 simulation with $k_\mathrm{f}/k_1 = 2.5$, which is inconsistent with the ideal case. Particularly worrisome is the case with explicit resistivity, which does show an effective resistivity that is larger than what is put in, and there is rapid magnetic helicity production early on.

All these features – the discontinuous dependence on resolution, the oscillatory behavior in some cases, and the spurious magnetic helicity production at early times – suggest that the ideal state may not be well defined and that different types of solutions may emerge instead, at least in this specific case of an ideal MHD solver based on the divergence-cleaning eight-wave scheme. The behavior expected from the resistive evolution, as reproduced by the PENCIL CODE, is not a typical outcome of ideal simulations, except for some cases of low resolution, or with explicitly added magnetic diffusivity. How generic this result is, however, remains open. It would therefore be interesting to subject the problem discussed in the present paper as a benchmark to other types of codes. For codes that are kept numerically stable with some type of explicit magnetic diffusion, e.g., through a modified scale dependence such as magnetic hyperdiffusion, the final outcome can in principle be predicted quantitatively, as was done by Brandenburg & Sarson (2002). However, there could well be other schemes with quite different behaviors that have not yet been anticipated.

In the MHD solver invoked here in `FLASH`, the constraint $\boldsymbol{\nabla} \cdot \boldsymbol{B} = 0$ is solved through a divergence cleaning algorithm (Brackbill & Barnes 1980). By calculating derivatives with a sixth order finite difference scheme, we have verified that $\langle (\boldsymbol{\nabla} \cdot \boldsymbol{B})^2 \rangle / \langle \boldsymbol{J}^2 \rangle$ stays of the order of 10^{-4}, and does not increase. In the PENCIL CODE, by contrast, $\boldsymbol{\nabla} \cdot \boldsymbol{B} = 0$ is ensured by solving directly for $\boldsymbol{A}$. It might therefore be possible that the artificial magnetic helicity production in `FLASH` could be related to the use of the divergence cleaning algorithm. This is not obvious, however, because the contribution from a gradient correction to $\boldsymbol{B}$ should not produce magnetic helicity if $\boldsymbol{A}$ is computed in the Coulomb gauge. In any case, as the resolution is increased from 48^3 to 64^3, not only does the fractional helicity production during the non-resistive phase decrease, but also the rate of magnetic helicity production decreases. This suggests that at sufficiently high numerical resolution, magnetic helicity should be well conserved also in `FLASH`. It would be interesting to see how magnetic helicity production is affected by using instead the constrained transport algorithm (Evans & Hawley 1988).

5. CONCLUSIONS

We have seen that, at low resolution, an ideal MHD code such as the eight-wave scheme in `FLASH` can reproduce certain aspects of resistive low magnetic Reynolds number dynamos, although other aspects are still not entirely physical. For example, in a periodic system, the current helicity must approach zero at late times, but no such tendency is found in the present simulations (see Figure 8). Already at twice the resolution, however, the `FLASH` code gives no large-scale dynamo action at all. This is, in principle, in agreement with the infinite magnetic Reynolds number case, although the violation of magnetic helicity conservation at early times speaks against this. Real systems, on the other hand, are not fully homogeneous and cannot be described by periodic boundary conditions. This can lead to the occurrence of magnetic helicity fluxes (Blackman & Field 2000).

It would in future be interesting to extend our studies to systems that do possess a magnetic helicity flux (Hubbard & Brandenburg 2010; Mitra et al. 2010; Del Sordo et al. 2013; Brandenburg 2018). In view of our results, however, we cannot take it for granted that the magnetic field evolution in poorly resolved systems reproduces in any way the behavior expected for a standard Spitzer resistivity.

Of course, modern simulations tend to have a numerical resolutions much larger than 32^3, but at the same time, one usually captures much more complex physical processes covering a large range of length scales. At the smallest scale, therefore, the effective resolution is again just barely enough to resolve the details of magnetic structures. In this sense, our work has implications for the study of dynamos with ideal codes at any resolution. It remains therefore mandatory to subject any dynamo simulation to a proper convergence test with fixed explicit resistivity.

This work was performed at the Aspen Center for Physics, which is supported by National Science Foundation grant PHY-1607611. We enjoyed the stimulating atmosphere during the Aspen program on the Turbulent Life of Cosmic Baryons. This research was supported in part by the Astronomy and Astrophysics Grants Program of the National Science Foundation (grants 1615100 and 1715876).

APPENDIX

A. LATE SATURATION PHASE

To understand the origin of Equation (2), we use Equation (1), introduce mean fields, $\overline{\boldsymbol{B}}$, as suitably defined planar averages, and define fluctuations correspondingly as $\boldsymbol{b} = \boldsymbol{B} - \overline{\boldsymbol{B}}$, and likewise for the magnetic vector potential $\boldsymbol{a} = \boldsymbol{A} - \overline{\boldsymbol{A}}$ and the magnetic current density $\boldsymbol{j} = \boldsymbol{J} - \overline{\boldsymbol{J}}$, respectively Equation (1) then becomes

$$\frac{\mathrm{d}}{\mathrm{d}t}\langle\overline{\boldsymbol{A}}\cdot\overline{\boldsymbol{B}}\rangle = -2\eta\langle\overline{\boldsymbol{J}}\cdot\overline{\boldsymbol{B}}\rangle - 2\eta\langle\boldsymbol{j}\cdot\boldsymbol{b}\rangle, \tag{A1}$$

where we have ignored the time derivative of $\langle\boldsymbol{a}\cdot\boldsymbol{b}\rangle$, because the small-scale magnetic field has saturated at $t = t_{\rm sat}$; (Figure 1) is approximately constant during the late saturation phase, $t > t_{\rm sat}$. Next, we approximate $\langle\overline{\boldsymbol{A}}\cdot\overline{\boldsymbol{B}}\rangle \approx -\langle\overline{\boldsymbol{B}}^2\rangle/k_1$, $\langle\overline{\boldsymbol{J}}\cdot\overline{\boldsymbol{B}}\rangle \approx -\langle\overline{\boldsymbol{B}}^2\rangle k_1$, and $\langle\boldsymbol{j}\cdot\boldsymbol{b}\rangle \approx +\langle\boldsymbol{b}^2\rangle k_{\rm f}^{\rm eff}$. Finally, we approximate $\langle\boldsymbol{b}^2\rangle/8\pi \approx \mathcal{E}_{\rm K}$, and obtain

$$\left(2\eta k_1^2 + \frac{\mathrm{d}}{\mathrm{d}t}\right)\mathcal{E}_{\rm M} = 2\eta k_1 k_{\rm f}^{\rm eff}\mathcal{E}_{\rm K}, \tag{A2}$$

which can be integrated to yield Equation (2).

REFERENCES

Benzi, R., Biferale, L., Fisher, R. T., et al. 2008, PhRvL, 100, 234503

Berger, M., & Field, G. B. 1984, JFM, 147, 133

Blackman, E. G., & Brandenburg, A. 2002, ApJ, 579, 359

Blackman, E. G., & Field, G. B. 2000, MNRAS, 318, 724

Brackbill, J. U., & Barnes, D. C. 1980, JCoPh, 35, 426

Brandenburg, A. 2001, ApJ, 550, 824

Brandenburg, A. 2010, MNRAS, 401, 347

Brandenburg, A. 2018, AN, 339, 631

Brandenburg, A., & Sarson, G. R. 2002, PhRvL, 88, 055003

Childress, S. & Gilbert, A. G. 1995, Stretch, twist, fold: the fast dynamo (Berlin: Springer)

Del Sordo, F., Guerrero, G., & Brandenburg, A. 2013, MNRAS, 429, 1686

Derigs, D., Winters, A. R., Gassner, G. J., & Walch, S. 2016, JCoPh, 317, 223

Eswaran, V., & Pope, S. B. 1988, PhFl, 31, 506

Evans, C. R. & Hawley, J. F. 1988, ApJ, 332, 659

Fryxell, B., Olson, K., Ricker, P., et al. 2000, ApJS, 131, 273

Haugen, N. E. L., Brandenburg, A., & Dobler, W. 2004, PhRvE, 70, 016308

Hubbard, A., & Brandenburg, A. 2010, GApFD, 104, 577

Ji, H. 1999, PhRvL, 83, 3198

Kahniashvili, T., Brandenburg, A., Tevzadze, A. G., & Ratra, B. 2010, PhRvD, 81, 123002

Mitra, D., Candelaresi, S., Chatterjee, P., Tavakol, R., & Brandenburg, A. 2010, AN, 331, 130

Moffatt, H. K., & Proctor, M. R. E. 1985, JFM, 154, 493

Schekochihin, A. A., Cowley, S. C., Taylor, S. F., Maron, J. L., McWilliams, J. C. 2004, ApJ, 612, 276

Seehafer, N. 1996, PhRvE, 53, 1283

Sur, S., Pan, L., & Scannapieco, E. 2014, ApJ, 784, 94

Vainshtein, S. I., & Zeldovich, Ya. B. 1972, SvPhU, 15, 159